ACS APPLIED NANO MATERIALS

www.acsanm.org Article

Nanoscale Mapping of Light Emission in Nanospade-Based InGaAs Quantum Wells Integrated on Si(100): Implications for Dual Light-Emitting Devices

Lucas Güniat,[‖] Nicolas Tappy,[‖] Akshay Balgarkashi, Titouan Charvin, Raphaël Lemerle, Nicholas Morgan, Didem Dede, Wonjong Kim, Valerio Piazza, Jean-Baptiste Leran, Luiz H. G. Tizei, Mathieu Kociak, and Anna Fontcuberta i Morral*

Cite This: https://doi.org/10.1021/acsanm.2c00507 Read Online

ACCESS | Metrics & More | Article Recommendations | Supporting Information

ABSTRACT: III−V semiconductors outperform Si in many optoelectronics applications due to their high carrier mobility, efficient light emission and absorption processes, and the possibility to engineer their band gap through alloying. However, complementing Si technology with III−V semiconductors by integration on Si(100) remains a challenge still today. Vertical nanospades (NSPDs) are quasi-bi-crystal III−V nanostructures that grow on Si(100). Here, we showcase the potential of these structures in optoelectronics application by demonstrating InGaAs heterostructures on GaAs NSPDs that exhibit bright emission in the near-infrared region. Using cathodoluminescence hyperspectral imaging, we are able to study light emission properties at a few nanometers of spatial resolution, well below the optical diffraction limit. We observe a symmetric spatial luminescence splitting throughout the NSPD. We correlate this characteristic to the structure's crystal nature, thus opening new perspectives for dual wavelength light-emitting diode structures. This work paves the path for integrating optically active III−V structures on the Si(100) platform.

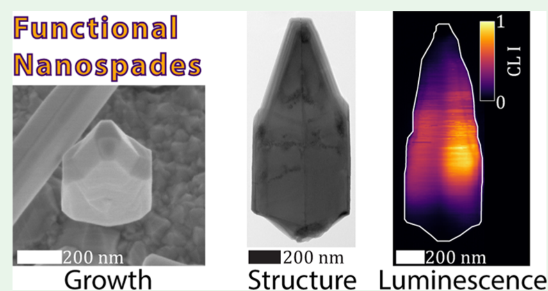

KEYWORDS: *nanospades, GaAs nanowires, vertical growth, InAs, quantum well, cathodoluminescence, hyperspectral imaging*

INTRODUCTION

As researchers look for material systems to meet today's advancing technological needs, one of the key challenges is the integration of emerging materials within established platforms. The semiconductor field does not deviate from this rule. III−V semiconductor alloys exhibit outstanding performances in applications such as solar cells,[1−3] transistors,[4,5] and infrared and terahertz detectors.[6] However, their monolithic integration on Si wafers is still challenging and limit their upscalability. Difficulties inherent to heteroepitaxy need to be overcome, such as polarity and lattice mismatch.[7] One way to tackle these issues is to grow III−V nanowires (NWs) on Si.[8−10] Nanosized objects show an increased capacity for elastic strain relaxation and also possess a very small footprint that protects them from antiphase boundaries.[11] NWs are great templates for the growth of quantum heterostructures[12−14] and open perspectives in fields such as quantum computing[15−17] and optoelectronics.[18,19] Despite their promises, vertical III−V NWs have proven very challenging to obtain on Si(100) since a {111}B growth direction is energetically preferred.[20] In the last years, it has been the principal difficulty to combine the advantages of the NW architecture and the CMOS-compatible Si(100) platform.

Recently, we have demonstrated the integration of vertical nanostructures on Si(100) by the growth of vertical nanospades (NSPDs).[21] NSPDs are very pure crystalline GaAs vertical nanostructures on Si(100) nanopillars. They are obtained using the self-catalyzed vapor−liquid−solid (VLS) mechanism in a molecular beam epitaxy (MBE) system. Figure 1a−d shows a summary of the growth process. Compared with the self-catalyzed GaAs NWs that usually grow in a ⟨111⟩B direction, NSPDs are bi-crystals with mirrored {111} growth planes. The two {111} planes have a twinning relationship in the [110] direction perpendicular to the growth axis and therefore exhibit different polarities at the growth front.[21] As a consequence, NSPDs are [100]-oriented structures born from the joint growth of a {111}A plane and a {111}B plane. Despite the difference in growth kinetics between {111}A and {111}B planes, NSPDs remain morphologically symmetrical

Received: February 2, 2022
Accepted: April 4, 2022

Downloaded via 86.238.178.41 on April 16, 2022 at 16:15:14 (UTC).
See https://pubs.acs.org/sharingguidelines for options on how to legitimately share published articles.

ACS Publications © XXXX The Authors. Published by American Chemical Society

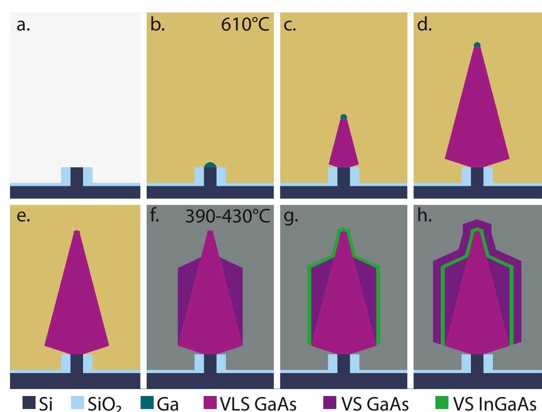

Figure 1. Comic strip of the growth process viewed in the cross-section: (a) Si nanopillar, (b) Ga droplet deposition, (c) NSPD during VLS growth, (d) fully grown NSPD, (e) Ga droplet consumption, (f) VS growth at lower temperature, change of the KCS, (g) InGaAs QW integration, and (h) VS GaAs capping.

due to the growth being completely limited by the nucleation at the twin boundary.

This study shows their capacity to serve as templates for integrating GaAs/InAs/GaAs quantum heterostructures directly on Si(100) using additional vapor−solid (VS) growth steps at lower temperature, as displayed in Figure 1e−h. We study the optoelectronic behavior of a GaAs/InGaAs/GaAs core−shell NSPD system and link it with morphological aspects, such as shell thickness, NSPD stem crystal polarity, and In concentration. Finally, we comment on the future of III−V implementation on Si(100).

■ RESULTS AND DISCUSSION

The twin plane crosses the entire NSPD and divides it into two symmetrical domains that are visible in bright-field transmission electron microscopy (BF-TEM) micrographs (see the Supporting Information). The crystal rotation through that twin is 60° in the direction orthogonal to the twin plane (ortho-twin[22]) and does not form a polarity inversion. Figure 2a shows a scanning electron micrograph of the NSPD, as-grown on a Si(100) substrate. The Ga droplet catalyst is visible on top of the nanostructure. The elongated hexagonal cross-section typical of NSPDs is clearly visible, with two {110} vertical sidewalls, front and back on this figure, and four slanted {110} sidewalls, left and right. It is worth noting that NSPDs are oriented with respect to the [100] substrate direction but do not, internally, grow along a crystalline [100] direction. In this work, every time the [100] NSPD growth direction is mentioned, we refer to the apparent [100] orientation of the full NSPD. For a more detailed analysis of the growth mechanisms and initiation of NSPDs, please refer to our previous study on NSPDs.[21]

We use GaAs NSPDs on Si(100) nanopillars as a core for the growth of III−V heterostructures. Early in our experiments, we observed that additional VS shell growth in the MBE[23] resulted in the transformation of the NSPD tilted sidewalls observed in Figure 2a into vertical sidewalls on a substantial portion of the nanostructure, as seen in Figure 2b. The cross-section shape changes from hexagonal to rectangular, as seen in Figure 2c (NSPD scanning electron micrograph top-view). We attribute this to the different growth temperature and As_4 partial pressure that, together, kinetically favors vertical fronts, that is, changes the kinetic crystal shape (KCS) of the system.[24] The crystalline orientation of these facets is discussed below.

Growing the first GaAs shell for long enough, that is, generating the change of the KCS, before growing an InGaAs/GaAs shell opens perspectives for growing rectangular InGaAs quantum wells. In such wells, it is predicted that quantum states at the corners will be energetically distinct from quantum states in the facets.[17,25,26] This should result in charge carrier confinement at the corners, meaning that an NSPD could host four quantum wires robust to external perturbations. With this in mind, we show the target cross-section of the grown

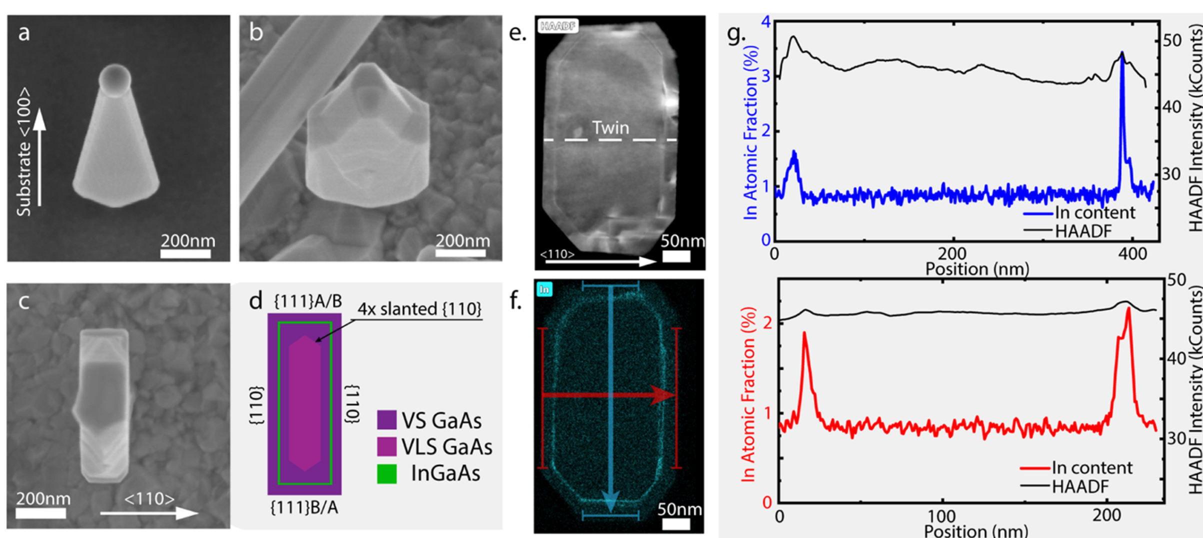

Figure 2. SEM micrographs of (a) as-grown GaAs NSPD on Si(100) (20° tilted view), (b) capped NSPD (20° tilted view) with a 390 °C shell growth temperature, (c) top-view of a capped NSPD from the same growth, showing the rectangular base cross-section, (d) schematic of the inner layers of the studied NSPDs, (e) STEM−HAADF image of an NSPD cut by ultramicrotomy, (f) STEM EDX map showing the In-rich shell, (g) average line scans of the In concentration in (f) red corresponds to the left−right scan, and blue corresponds to the top−down scan. On the right axis, the HAADF intensity counts are shown.

structure in Figure 2d. A GaAs NSPD core, shown in light purple in Figures 1c and 2d, is grown at a higher temperature (610 °C) and a lower As partial pressure (1.5×10^{-6} Torr) for a V/III ratio of 12 until reaching a length of 1.5 μm, Figure 1d. The As_4 partial pressure is then increased up to 1×10^{-5} Torr, and the Ga shutter is closed for 30 min in order to stop the VLS growth process and consume the Ga droplet, Figure 1e. The temperature is also dropped significantly for entering the VS growth regime. The first GaAs shell is grown, shown in dark purple on Figure 1f, forming the rectangular vertical facets. Pure InAs is sent for a relatively short time with a decreased As_4 flux of 5×10^{-6} Torr and a V/III ratio of 55 (light green), Figure 1g, before reinitiating a GaAs capping shell growth, Figure 1h. We varied the VS growth temperature from 430 to 390 °C. We expect a substantial interdiffusion of elements, leading to an InGaAs nanostructure with an In-rich region where InAs was deposited and Ga-rich regions for the core NSPD and the two capping GaAs-grown shells.[27] For high shell growth temperatures (430 and 420 °C), we expect InGaAs clustering or accumulation at defects such as stacking faults or dislocations. This can be explained by InAs strain relaxation and a high In diffusion length, leading to the nucleation of three-dimensional structures.[27] For samples with lower shell growth temperature (400 and 390 °C), we observed a more uniform GaAs/InGaAs/GaAs heterostructure.

Cross-sections of NSPD heterostructures grown as a GaAs NSPD core and GaAs/InGaAs/GaAs shells grown at 400 °C were prepared using ultramicrotomy.[28] Analysis of the heterostructure was performed using high-angle annular dark-field (HAADF) scanning transmission electron microscopy (STEM). This technique allows us to obtain images with atomic number contrast (Z contrast). Figure 2e shows an HAADF STEM image of the NSPD's cross-section. The contrast allows us to identify the presence of a thin well of higher atomic number elements in the structure. We further study it using STEM energy-dispersive X-ray spectroscopy (EDX). Figure 2f shows the EDX map of In distribution in the sample. We observe the presence of a thin In-rich thin layer in the shell structure. The In-rich layer is uniform and conformal to the NSPD core, as expected from a low-temperature shell growth. In the STEM EDX and HAADF measurement, we observe an octagonal shell morphology, different from the ideal structure cross-section of Figure 2d. We believe that the cross-section studied originates from an upper part of the NSPD, where the slanted sidewalls are not completely kinetically supplanted by the newly vertical sidewalls, similar to the work by Fonseka et al. on ⟨100⟩-oriented InP NWs.[29]

Figure 2g shows line scans of In composition averaged over perpendicular sidewall pairs. The red curve corresponds to a left−right scan and the blue curve corresponds to a top−down scan in image f. It allows us to attempt the quantification of the In concentration in the target quantum well. The left−right scan (red curve) shows two peaks of approximately equal heights at 1.90 ± 0.05 and 2.2 ± 0.05% In composition, respectively. Their full-width at half-maximum (fwhm) values are 3 and 4.5 nm, respectively. The top−down scan (blue) shows two peaks of relatively different heights at 1.5 ± 0.08 and 3.5 ± 0.08%, respectively. Their fwhm values are, respectively, 13.40 ± 0.66 and 4.00 ± 0.18 nm (evaluated from Gaussian fits). These values could show a difference in the InGaAs well width and/or In composition between the two sides of the NSPD, more specifically the two short sides. This difference could also be a measurement artefact, either caused by an STEM misalignment or damage during ultramicrotomy. In fact, measuring integrated peak areas does not reveal a pronounced difference between red and blue curves. Unveiling compositional differences between each side of an NSPD would require a more advanced study such as atom probe tomography (APT).[30] Instead, we adopt a functional approach by studying the asymmetry on the optoelectronic properties of NSPDs using spatially resolved spectroscopy techniques.

NSPDs were transferred flat on a TEM grid and studied in a cathodoluminescence-dedicated scanning electron microscope (SEM-CL, Attolight Allalin). The working principle of SEM-CL consists of probing the sample using the highly focused electron beam in an SEM system and gathering photons emitted from the excited area and surrounding region. Thereby, the spatial resolution is limited by the interaction volume of the electrons within the structure and the diffusion of the excited electron−hole pairs.[31,32] Typically, the emitted light is spectrally analyzed, and a powerful SEM-CL measurement scheme consists of acquiring one emission spectrum at each location of a two-dimensional scanned region, called a hyperspectral (HS) map. This map can be correlated with the secondary electron (SE) image of the same area. Often, the sample is kept at cryogenic temperature during the measurement to enhance emission efficiency, passivate nonradiative defects, and obtain sharper emission lines.

Hereafter, we discuss the SEM-CL results obtained on samples with shells grown at 390 °C. Samples grown at a higher shell temperature (430 and 420 °C) exhibited localized emissions throughout the NSPD, as we previously observed in NW-based heterostructures,[27] due to In clustering and interdiffusion. SEM-CL analysis of such samples can be found in the Supporting Information.

Figure 3a depicts the measured emission spectrum. The NSPD heterostructures display a rich luminescence signal between 1.225 and 1.375 eV, expected of $In_xGa_{1-x}As$ emitting features such as quantum dots and quantum wells. 1.225 eV would correspond to the band gap of bulk $In_{0.2}Ga_{0.8}As$ and 1.375 eV to $In_{0.09}Ga_{0.91}As$. Carrier confinement effects, as found in quantum wells and quantum dots, would further contribute to a blue shift in the emission spectrum. This indicates that EDX measurements are strongly underestimating the actual In content of the radial shell, as expected from EDX measurements misaligned with respect to the zone axis. GaAs band-edge emission is undetectable, indicating dominant capture of the carriers in the InGaAs layer. The broadband spectrum is shown in the Supporting Information.

The numerous emission peaks indicate that In composition and well thickness vary within the structure. We modeled the data by fitting the principal peaks of the signal with Lorentzian lineshapes (23 in total) for each acquired spectra, that is, each point of the HS map. The average spectrum of the model is indicated as the black line in Figure 3a. Qualitatively, its good agreement with the experimental data (black dots on Figure 3a.) confirms that the emission fingerprint of the NSPD arises from the combination of a finite number of narrow emission lines. The complete set of fit results is available in the Supporting Information.

The SE image in Figure 3b shows that the bottom half of this NSPD exhibits vertical sidewalls on both sides, in similarity to Figure 2b. The top half of the NSPD shows rough converging sidewalls. We believe that the top half GaAs shell grew conformally to the NSPD core. The InGaAs section on the top half is thus expected to show irregular thicknesses

https://doi.org/10.1021/acsanm.2c00507
ACS Appl. Nano Mater. XXXX, XXX, XXX−XXX

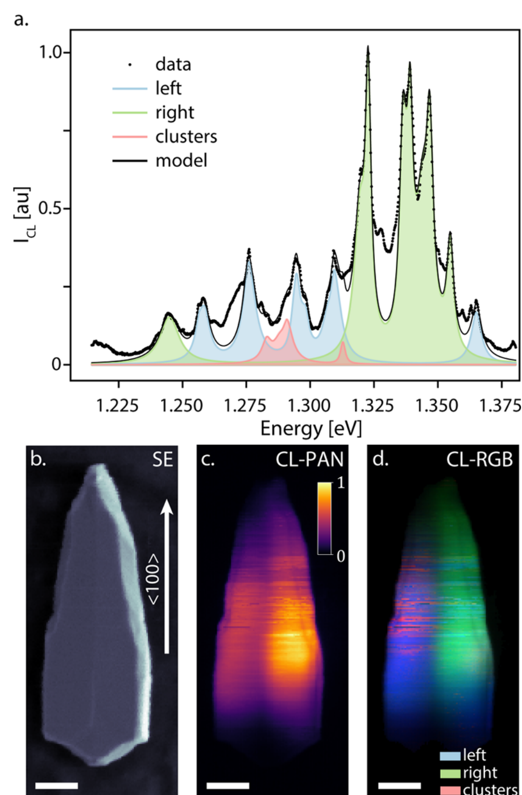

Figure 3. CL measurements obtained on an NSPD with a 390 °C shell growth temperature. (a) Average spectra showing the raw data, the fitted average model, and the three emission groups as green, blue, and red, respectively. (b) SE image of the measured NSPD. (c) Normalized panchromatic map of the signal. (d) False-colors RGB map of the three emission groups. Scale bar is 200 nm.

and compositions. The key elements that permit extended vertical sidewalls still need to be systematically assessed.

The panchromatic CL signal, Figure 3c, indicates that the entire structure exhibits emission intensity variations. The base emits a lower intensity, which is consistent with our previous work[21] showing that the crystalline structure of the NSPD has a higher defect concentration in this zone, including a five-fold twinning region, dislocations, and polarity inversion. The end of the structure also shows lower emission intensity, consistent with the consumption of the Ga droplet forming a defected region.[27] The NSPD's geometrical axis shows a decrease in intensity correlated to the presence of the central twin. We believe that the mentioned defects act as nonradiative recombination centers and locally decrease luminescence efficiency. Evaluating the total luminescence efficiency is challenging due to the nontrivial radiation patterns[33] and complex charge carriers dynamics including surface effects[34] in NSPDs. Solving these remains outside of the scope of this article. The Supporting Information contains quantitative considerations on the signal intensity.

To interpret the luminescence signal in more detail, we observe the amplitude maps of each peak fitted in the model. Three distinct groups of peaks arise, corresponding to different emission behavior in the nanostructure. Some present relatively uniform emission and are dominant either in the left (left group) or in the right (right group) of the NSPD. Finally, some other peaks present highly localized emission in specific locations of the top half of the NSPD (clusters group), where they are overwhelmingly bright compared to all other emission peaks. However, because of this localized character, their contribution to the mean spectrum signal is low. The three groups are indicated in Figure 3a as blue, green, and red filled curves, respectively. The left (blue) group is composed of seven peaks between 1.250 and 1.315 eV and one peak at 1.365 eV. The right (green) group is composed of seven peaks between 1.315 and 1.355 eV and one peak at 1.244 eV. The clusters (red) group is composed of three peaks between 1.270 and 1.290 eV and one at 1.312 eV. Figure 3d shows the total intensity of each peak group as a false-RGB map (CL-RGB), highlighting their peculiar intensity distribution.

This analysis highlights the anisotropy in the electrical properties of the NSPD heterostructure. The left−right asymmetry in SEM-CL emission correlates with the NSPD crystalline structure: specifically, the central twin. The emission energy changing from left to right sides evidences a change in the morphological and/or compositional properties of the InGaAs section. Because of the asymmetric In incorporation observed using EDX, it is tempting to associate these to emission in the side quantum wells growing on 111A/B sides. Some signal intermixing remains, especially in the bottom half region with vertical sidewalls. This is consistent with the emission from the top quantum well, integrated on 110 sides of the NSPD. The highly localized emission behavior from the clusters group is characteristic of ensembles of low-dimensionality (quantum dots) emitters in the nanostructure shell, for instance, InGaAs clusters forming at the surface of the rough, conformal GaAs shell.[27,35]

The excitation volume and large amount of energy deposited by 2 keV electrons in the sample do not permit us to identify local InGaAs shell composition or thickness variations. Hence, we switched to CL measurements in a scanning transmission electron microscope (modified Nion Hermes, called Chroma-TEM) that permits a spatial selectivity as high as a few nanometers thanks to the much smaller interaction volume for higher kinetic energy electrons (60 keV compared to 2 keV).[36] We performed such measurements on NSPD horizontal cuts obtained using ultramicrotomy. Ultramicrotomy allows us to isolate the bottom half of the NSPD and study it in a cross-section configuration. This way, we expect a higher homogeneity of the InGaAs shell and to avoid InGaAs clusters emission. A representative measurement can be seen in Figure 4. Figure 4a shows the live HAADF micrograph of the NSPD cross-section. The presence of the rectangular corners on the left side confirms that we successfully transferred the lower part of the nanostructure. The right part appears damaged by the cutting procedure as the corners have been partially separated from the rest of the cross-section. The central twin is visible as a bright line in the middle of the structure, indicated by arrows. We confirm that such a contrast is not a measurement artefact as the scanning angle is clearly visible from the streaks of the image and is close to 45° of the twin orientation. Figure 4b shows the measurement's signal integrated on the 1.200−1.350 eV range. It exhibits a decrease in the overall intensity on the right side of the twin. This is consistent with the visible damage on Figure 3a. We also see a decrease in intensity on the top center of the structure, where a protrusion is visible on the HAADF image of 4a. We attribute this to the presence of a growth defect at the twin boundary during shell growth, which allows for nonradiative recombination. The same phenomenon could explain the decrease in intensity close to the central twin systematically observed using SEM-CL.

https://doi.org/10.1021/acsanm.2c00507
ACS Appl. Nano Mater. XXXX, XXX, XXX−XXX

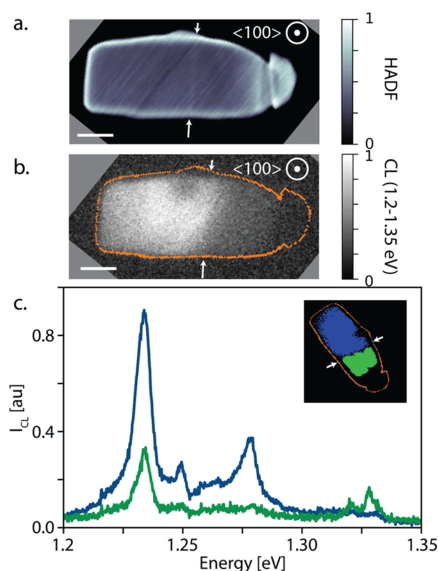

Figure 4. STEM-CL measurements performed on an ultramicrotomy cut of a GaAs/InGaAs/GaAs NSPD heterostructure. (a) High-angle dark field micrograph of the NSPD's cross-section, depicting the shell's rectangular nature. (b) CL panchromatic map of the same cut. (c) Average spectra of the left side of the NSPD in blue and the right side in green. Scale bar is 100 nm.

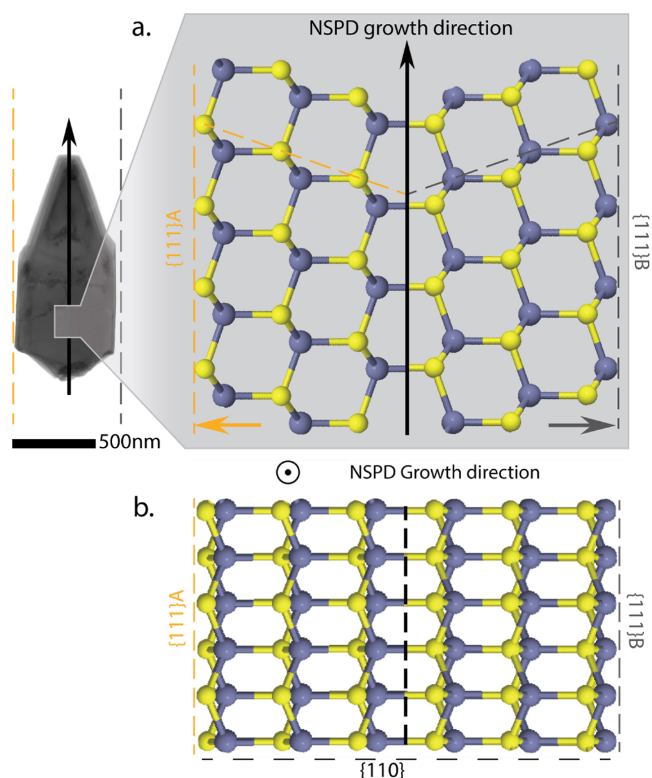

Figure 5. Atomistic model of the NSPD crystal structure. (a) BF TEM image of an NSPD with the crystal side view. (b) Crystal top view. The central twin is represented by a dotted line.

Figure 4c shows the average intensity spectra for the left side (blue) and the right side (green) around the NSPD's central twin. We observe an intensity variation between the blue and green curves that is consistent with the damage observed on the NSPD's right side. The emission energy range, that is, 1.200−1.340 eV, is comparable to the SEM-CL measurements. The number of emission peaks is drastically reduced. We attribute this to the absence of the NSPD's top half InGaAs clusters in STEM-CL measurements, proving the technique's efficiency to selectively probe the InGaAs conformal shell. However, the signal-to-noise ratio is much lower due to the low excitation density, higher sample temperature (130 vs 10 K), and mechanical damage from the microtomy. Consequently, modeling the signal is not possible. STEM-CL measurements require using amplified detectors (EMCCD) and averaging signal over multiple scanned points to retrieve the spectral features of interest.

The blue side of Figure 4c shows two emission peaks at 1.250 and 1.275 eV, while the green side shows two emission peaks at 1.320 and 1.330 eV. These emission groups are consistent with, respectively, the blue and green emission groups from the SEM-CL measurements of Figure 3. By only probing the InGaAs conformal shell, STEM-CL measurements confirms a morphological and/or compositional change in our GaAs/InGaAs/GaAs heterostructure. The emission peak at 1.230 eV is present on both sides of the NSPD's cross-section. Again, this is consistent with a side-invariant InGaAs feature, such as a quantum well on the {110} side. We will now focus on the atomic structure of the NSPD and identify which InGaAs features change in the morphology and/or composition and which do not.

To illustrate this, we show in Figure 5 an atomistic model of the internal structure of the NSPD far from the base. We can see that the ⟨100⟩ growth direction of the NSPD is only referring to the substrate orientation and not the internal orientation of the crystal domains. In fact, the NSPD VLS growth front is composed by a {111}A plane and a {111}B plane, visible, respectively, in orange and gray in the figure. Figure 5a also shows that due to the ⟨100⟩ orientation of the central twin, the left and right vertical sidewalls of the NSPD are {111} planes of different polarities, highlighted by the orange and gray arrows, respectively. The left side corresponding to the {111}A VLS growth front also exhibits a {111}A vertical sidewall. Similarly, the right side corresponding to the {111}B VLS growth front exhibits a {111}B vertical sidewall.

Figure 5b shows a top view of the NSPD with the central twin plane shown as a dotted line. We can observe the left {111}A vertical sidewall and the right {111}B vertical sidewall. Top and bottom vertical sidewalls on this image correspond to nonpolar {110} vertical planes. The NSPD platform thus offers the full variety of atomic polarities during growth. The literature shows that the kinetics of III−V VS growth is polarity-dependant.[37−39] Specifically, this is true for the growth of InAs heterostructures on GaAs NWs.[39] Guo et al. explain the polarity-driven effect by a difference in lattice strain relaxation between the A-polar facet and the B-polar facet during In incorporation. Since every group III element needs to form three bonds on the {111}A surface and only one on {111}B, the InAs higher lattice constant leads to a preferential In incorporation at the B-polar surface.

This polarity-driven In incorporation mechanism can explain the left/right asymmetry in CL measurements, observed in NSPDs with shells grown at 400 and 390 °C. The {111}B vertical sidewall appears preferential for In incorporation, leading to a decreased band gap and a red-shifted emission peak. Thus, the right group of peaks in Figures 3 and 4, shown in green, is consistent with a {111}B vertical sidewall. The left group, shown in blue, is consistent with a complementary

{111}A sidewall. On the other hand, the two 110 vertical sidewalls are identical on both sides of the twin. This supports the presence of a side-invariant emission, similar to the peak seen in Figure 4c and the intermixing in Figure 3d. This opens perspectives for single free-standing III−V heterostructures on Si exhibiting three distinct square quantum wells with distinct optical responses. Eventually, one could use this to design a multiwavelength light-emitting diode (LED) structure. By selectively contacting each side, one could selectively emit the required wavelength.

■ CONCLUSIONS

In this study, we show the potential for integrating InGaAs/GaAs quantum wells in core−shell GaAs NSPD heterostructures. VS shell growth between 390 and 430 °C were studied. At the lowest shell growth temperatures, we obtain a continuous InGaAs thin shell, avoiding In clustering and interdiffusion on a large portion of the NSPDs. We subsequently studied the optoelectronic and structural properties of the InGaAs heterostructures and linked them with the unique crystalline structure of NSPDs using SEM-CL and STEM-CL spectroscopy. We observe a bright emission of the nanostructures with groups of emission peaks between 1.225 and 1.375 eV, assimilable with bulk $In_xGa_{1-x}As$ with x between $x = 0.1$ and $x = 0.2$. We unveiled the potential presence of a dual emission due to a difference in polarity between each side of the NSPD. These results open perspectives for dual-LED nanostructures on Si where each side of the central twin could be excited separately at will. NSPD heterostructures being crystallographically complex structures, further developing the integration of QW in this platform would benefit from advanced optoelectronic and compositional characterization. For instance, power-dependent photoluminescence, APT or aberration-corrected HAADF STEM could provide valuable insights on the exact QW configurations in the system.[40]

■ EXPERIMENTAL SECTION

For EBL Pillars. A 2 min 600 W O_2 plasma treatment in a TEPLA GigaBatch system is performed on a 100 mm Si wafer for surface activation before exposing it via e-beam lithography using a Vistec EBPG5000ES, with a Dow Corning HSQ 006 (Hydrogen silsesquioxane) as a resist. The dose used is 2740 $\mu C/cm^2$ for all pillar diameters. The wafer is then developed using a commercial solution of Microposit MF CD26 for 2 min and rinsed sequentially with water, acetone, and propan-2-ol. A 2 min 600 W O_2 plasma treatment in a TEPLA GigaBatch is performed for further cross-linking the HSQ.

The wafer is then introduced in an Alcatel AMS200 DSE reactive ion etcher, where a customized recipe using SF_6 and C_4F_8 is used to etch back the substrate in the unpatterned regions, creating the pillars. A buffered hydrofluoric acid (7:1) bath is then used for 2 min to remove any trace of the resist. Thermal oxidation is then performed at 900 °C for a variable amount of time depending on the wanted oxide thickness. After the oxide growth, a 20 nm styrene methyl acrylate-based resist (ZEP) film is spin-coated and heated for 2 min at 180 °C for polymerization. The sample is inserted in an Oxford Plasmalab 80 PLUS system using a mixture of SF_6 and CHF_3 at 100 W plasma power for 40 s to uncover the pillars. 10 min of O_2 plasma treatment allows us to remove the resist, and a last cleaning process involving a 5 min acetone bath, a 2 min propan-2-ol bath, and a 35 s HF bath at 1% concentration makes the sample ready for growth.

The growths are conducted in a DCA MBE chamber. All the reported MBE growth temperatures are estimations of the substrate temperature. From measurements performed using an infrared camera on known standard GaAs samples, we estimate a difference of 130 °C between the set PID and the real temperature.

Ultramicrotomy. Structures were peeled-out from the substrate using an epoxy resin. The thin cross-sections were prepared using a Leica EM UC7 Ultramicrotome system at room temperature. A Diatome ultra 35° diamond knife was used to obtain smooth cross-sections. The thickness of each cross-section was 90 nm.

The samples were characterized via SEM using a Zeiss Merlin and via BF TEM/HAADF STEM using an FEI Talos. The SEM-CL measurements were performed using an Attolight Rosa 4634 SEM-CL microscope, with an electron beam of 2 keV and a sample temperature of 10 K. The spectroscopy setup consists of a 320 mm Czerny-Turner spectrometer with a 150 mm^{-1} grating and a cooled CCD (Andor Newton 920). In the CL HS map of Figure 2, a probe current of approximately 100 nA is used with a dwell time of 20 ms per spectral acquisition. STEM-CL measurements were performed at 60 kV in a modified Nion Hermes microscope equipped with a N2-cooled stage (sample temperature close to 130 K) and a CL add on (Attolight Mönch) fiber-coupled with a 320 mm Czerny and a Teledyne Princeton Instruments EMCCD. HS analysis was performed using the free and open-source python library hyperspy.[41]

Uncertainties of the In content measured using EDX were estimated from the variation of the baseline counts. For the measurement of the radial well fwhm based on the same EDX data, the uncertainty is estimated from the Gaussian fit results. Uncertainties on spectroscopic measurements are dominated by the repeatability of the Czerny-Turner spectrometers positioning, which translates to 0.1 meV on the determination of the line energies. The error on the spatial scale is inferior to 1% for all electron microscopy data presented here.

■ ASSOCIATED CONTENT

Supporting Information

The Supporting Information is available free of charge at https://pubs.acs.org/doi/10.1021/acsanm.2c00507.

Details of the TEM and CL analysis (PDF)

Complete set of fit results (ZIP)

■ AUTHOR INFORMATION

Corresponding Author

Anna Fontcuberta i Morral − *Laboratory of Semiconductor Materials, Institute of Materials, School of Engineering, École Polytechnique Fédérale de Lausanne, 1015 Lausanne, Switzerland; Institute of Physics, School of Basic Sciences, École Polytechnique Fédérale de Lausanne, 1015 Lausanne, Switzerland;* orcid.org/0000-0002-5070-2196; Email: anna.fontcuberta-morral@epfl.ch

Authors

Lucas Güniat − *Laboratory of Semiconductor Materials, Institute of Materials, School of Engineering, École Polytechnique Fédérale de Lausanne, 1015 Lausanne, Switzerland;* orcid.org/0000-0001-7883-4433

Nicolas Tappy − *Laboratory of Semiconductor Materials, Institute of Materials, School of Engineering, École Polytechnique Fédérale de Lausanne, 1015 Lausanne, Switzerland;* orcid.org/0000-0002-5466-5468

Akshay Balgarkashi − *Laboratory of Semiconductor Materials, Institute of Materials, School of Engineering, École Polytechnique Fédérale de Lausanne, 1015 Lausanne, Switzerland*

Titouan Charvin − *Laboratory of Semiconductor Materials, Institute of Materials, School of Engineering, École Polytechnique Fédérale de Lausanne, 1015 Lausanne, Switzerland*

https://doi.org/10.1021/acsanm.2c00507
ACS Appl. Nano Mater. XXXX, XXX, XXX−XXX

Raphaël Lemerle − *Laboratory of Semiconductor Materials, Institute of Materials, School of Engineering, École Polytechnique Fédérale de Lausanne, 1015 Lausanne, Switzerland*
Nicholas Morgan − *Laboratory of Semiconductor Materials, Institute of Materials, School of Engineering, École Polytechnique Fédérale de Lausanne, 1015 Lausanne, Switzerland*
Didem Dede − *Laboratory of Semiconductor Materials, Institute of Materials, School of Engineering, École Polytechnique Fédérale de Lausanne, 1015 Lausanne, Switzerland*
Wonjong Kim − *Laboratory of Semiconductor Materials, Institute of Materials, School of Engineering, École Polytechnique Fédérale de Lausanne, 1015 Lausanne, Switzerland*
Valerio Piazza − *Laboratory of Semiconductor Materials, Institute of Materials, School of Engineering, École Polytechnique Fédérale de Lausanne, 1015 Lausanne, Switzerland*
Jean-Baptiste Leran − *Laboratory of Semiconductor Materials, Institute of Materials, School of Engineering, École Polytechnique Fédérale de Lausanne, 1015 Lausanne, Switzerland*
Luiz H. G. Tizei − *Laboratoire de Physique des Solides, CNRS UMR 8502, Université Paris Sud XI, 91405 Orsay, France;* orcid.org/0000-0003-3998-9912
Mathieu Kociak − *Laboratoire de Physique des Solides, CNRS UMR 8502, Université Paris Sud XI, 91405 Orsay, France;* orcid.org/0000-0001-8858-0449

Complete contact information is available at:
https://pubs.acs.org/10.1021/acsanm.2c00507

Author Contributions

[‖]L.G. and N.T. contributed equally to this work

Notes

The authors declare no competing financial interest.

■ ACKNOWLEDGMENTS

L.G. thanks all the MBE team and also the CMi staff at EPFL without whom this study could not be possible. L.G. thanks Simon Escobar for the fruitful discussion on STEM EDX. L.G. and A.B. thank Colette Valloton for the help on ultramicrotomy. This project has received funding from the French Agence Nationale de la Recherche, grant number ANR-10-EQPX-50, from the European Commission Horizon 2020 Framework Program, grant number 823717-ESTEEM3, from the Swiss National Science Foundation National Centre of Competence in Research QSIT program, grant number IZLRZ2_163861, and from the Swiss National Science Foundation, grant numbers 200021_169908 and 40B2-0_176680.

■ ABBREVIATIONS

NSPD, nanospade
NW, nanowire
QW, quantum well
QWR, quantum well resonance

■ REFERENCES

(1) Suh, D.-I.; Lee, S.-Y.; Kim, T.-H.; Chun, J.-M.; Suh, E.-K.; Yang, O.-B.; Lee, S.-K. The Fabrication And Characterization Of Dye-sensitized Solar Cells With A Branched Structure Of ZnO Nanowires. *Chem. Phys. Lett.* **2007**, *442*, 348−353.

(2) Krogstrup, P.; Jørgensen, H. I.; Heiss, M.; Demichel, O.; Holm, J. V.; Aagesen, M.; Nygard, J.; Fontcuberta i Morral, A. Single-nanowire solar cells beyond the Shockley-Queisser limit. *Nat. Photonics* **2013**, *7*, 306−310.

(3) Wallentin, J.; Anttu, N.; Asoli, D.; Huffman, M.; Åberg, I.; Magnusson, M. H.; Siefer, G.; Fuss-Kailuweit, P.; Dimroth, F.; Witzigmann, B.; Xu, H. Q.; Samuelson, L.; Deppert, K.; Borgström, M. T. InP Nanowire Array Solar Cells Achieving 13.8% Efficiency by Exceeding the Ray Optics Limit. *Science* **2013**, *339*, 1057−1060.

(4) Cui, Y.; Wei, Q.; Park, H.; Lieber, C. M.; Park, H. Nanowire Nanosensors for Highly Sensitive and Selective Detection of Biological and Chemical Species. *Science* **2001**, *293*, 1289−1292.

(5) Chuang, S.; Gao, Q.; Kapadia, R.; Ford, A. C.; Guo, J.; Javey, A. Ballistic InAs Nanowire Transistors. *Nano Lett.* **2013**, *13*, 555−558.

(6) Peng, K.; Parkinson, P.; Gao, Q.; Boland, J. L.; Li, Z.; Wang, F.; Mokkapati, S.; Fu, L.; Johnston, M. B.; Tan, H. H.; Jagadish, C. Single n+-i-n+ InP Nanowires For Highly Sensitive Terahertz Detection. *Nanotechnology* **2017**, *28*, 125202.

(7) Tsao, J. Y. *Materials Fundamentals of Molecular Beam Epitaxy*; Elsevier, 2015; pp 215−220.

(8) Jam, R. J.; Beech, J. P.; Zeng, X.; Johansson, J.; Samuelson, L.; Pettersson, H.; Borgström, M. T. Embedded sacrificial AlAs segments in GaAs nanowires for substrate reuse. *Nanotechnology* **2020**, *31*, 204002.

(9) Munshi, A. M.; Dheeraj, D. L.; Fauske, V. T.; Kim, D. C.; Huh, J.; Reinertsen, J. F.; Ahtapodov, L.; Lee, K. D.; Heidari, B.; Van Helvoort, A. T. J.; Fimland, B. O.; Weman, H. Position-controlled Uniform GaAs Nanowires On Silicon Using Nanoimprint Lithography. *Nano Lett.* **2014**, *14*, 960−966.

(10) Kim, W.; Dubrovskii, V. G.; Vukajlovic-Plestina, J.; Tütüncüoglu, G.; Francaviglia, L.; Güniat, L.; Potts, H.; Friedl, M.; Leran, J.-B.; I Morral, A. F. Bistability of Contact Angle and Its Role in Achieving Quantum-Thin Self-Assisted GaAs nanowires. *Nano Lett.* **2018**, *18*, 49−57.

(11) Güniat, L.; Caroff, P.; i Morral, A. F. Vapor Phase Growth of Semiconductor Nanowires: Key Developments and Open Questions. *Chem. Rev.* **2019**, *119*, 8958−8971.

(12) Lauhon, L. J.; Gudiksen, M. S.; Wang, D.; Lieber, C. M. Epitaxial Core-shell And Core-multishell Nanowire Heterostructures. *Nature* **2002**, *420*, 57−61.

(13) Heigoldt, M.; Arbiol, J.; Spirkoska, D.; Rebled, J. M.; Conesa-Boj, S.; Abstreiter, G.; Peiró, F.; Morante, J. R.; i Morral, A. F. Long Range Epitaxial Growth Of Prismatic Heterostructures On The Facets Of Catalyst-free GaAs Nanowires. *J. Mater. Chem.* **2009**, *19*, 840.

(14) Heiss, M.; Fontana, Y.; Gustafsson, A.; Wüst, G.; Magen, C.; O'Regan, D. D.; Luo, J. W.; Ketterer, B.; Conesa-Boj, S.; Kuhlmann, A. V.; Houel, J.; Russo-Averchi, E.; Morante, J. R.; Cantoni, M.; Marzari, N.; Arbiol, J.; Zunger, A.; Warburton, R. J.; Fontcuberta i Morral, A. Self-assembled Quantum Dots In A Nanowire System For Quantum Photonics. *Nat. Mater.* **2013**, *12*, 439−444.

(15) Mourik, V.; Zuo, K.; Frolov, S. M.; Plissard, S. R.; Bakkers, E. P. A. M.; Kouwenhoven, L. P. Signatures Of Majorana Fermions In Hybrid Superconductor-semiconductor Nanowire Devices. *Science* **2012**, *336*, 1003−1007.

(16) Liu, Z.-h.; Li, R. Spin-relaxation Anisotropy In A Nanowire Quantum Dot With Strong Spin-orbit Coupling. *AIP Adv.* **2018**, *8*, 075115.

(17) Manolescu, A.; Sitek, A.; Osca, J.; Serra, L.; Gudmundsson, V.; Stanescu, T. D. Majorana States In Prismatic Core-shell Nanowires. *Phys. Rev. B: Condens. Matter Mater. Phys.* **2017**, *96*, 125435.

(18) Stettner, T.; Thurn, A.; Döblinger, M.; Hill, M. O.; Bissinger, J.; Schmiedeke, P.; Matich, S.; Kostenbader, T.; Ruhstorfer, D.; Riedl, H.; Kaniber, M.; Lauhon, L. J.; Finley, J. J.; Koblmüller, G. Tuning Lasing Emission toward Long Wavelengths in GaAs-(In,Al)GaAs Core-Multishell Nanowires. *Nano Lett.* **2018**, *18*, 6292−6300.

(19) Mayer, B.; Rudolph, D.; Schnell, J.; Morkötter, S.; Winnerl, J.; Treu, J.; Müller, K.; Bracher, G.; Abstreiter, G.; Koblmüller, G.;

Finley, J. J. Lasing from individual GaAs-AlGaAs core-shell nanowires up to room temperature. *Nat. Commun.* **2013**, *4*, 1−7.

(20) Ambrosini, S.; Fanetti, M.; Grillo, V.; Franciosi, A.; Rubini, S. Self-catalyzed GaAs nanowire growth on Si-treated GaAs(100) substrates. *J. Appl. Phys.* **2011**, *109*, 094306.

(21) Güniat, L.; Martí-Sánchez, S.; Garcia, O.; Boscardin, M.; Vindice, D.; Tappy, N.; Friedl, M.; Kim, W.; Zamani, M.; Francaviglia, L.; Balgarkashi, A.; Leran, J.-B.; Arbiol, J.; Fontcuberta I Morral, A. III-V III-V Integration on Si(100): Vertical Nanospades. *ACS Nano* **2019**, *13*, 5833−5840.

(22) Karlsson, L. Transmission Electron Microscopy of III-V Nanowires and Nanotrees. Ph.D. Thesis, Centre for Analysis and Synthesis, 2007.

(23) Priante, G.; Ambrosini, S.; Dubrovskii, V. G.; Franciosi, A.; Rubini, S. Stopping and Resuming at Will the Growth of GaAs Nanowires. *Cryst. Growth Des.* **2013**, *13*, 3976−3984.

(24) Albani, M.; Bergamaschini, R.; Salvalaglio, M.; Voigt, A.; Miglio, L.; Montalenti, F. Competition Between Kinetics and Thermodynamics During the Growth of Faceted Crystal by Phase Field Modeling. *Phys. Status Solidi B* **2019**, *256*, 1−10.

(25) Sitek, A.; Torres, M. U.; Torfason, K.; Gudmundsson, V.; Bertoni, A.; Manolescu, A. Excitons in Core-Shell Nanowires with Polygonal Cross Sections. *Nano Lett.* **2018**, *18*, 2581−2589.

(26) Torres, M. U.; Sitek, A.; Erlingsson, S. I.; Thorgilsson, G.; Gudmundsson, V.; Manolescu, A. Conductance Features Of Core-shell Nanowires Determined By Their Internal Geometry. *Phys. Rev. B* **2018**, *98*, 085419.

(27) Balgarkashi, A.; Ramanandan, S. P.; Tappy, N.; Nahra, M.; Kim, W.; Güniat, L.; Friedl, M.; Morgan, N.; Dede, D.; Leran, J. B.; Couteau, C.; i Morral, A. F. Facet-driven formation of axial and radial In(Ga)As clusters in GaAs nanowires. *J. Opt.* **2020**, *22*, 084002.

(28) Watson, D. C.; Martinez, R. V.; Fontana, Y.; Russo-Averchi, E.; Heiss, M.; I Morral, A. F.; Whitesides, G. M.; Lončar, M. Nanoskiving core-shell nanowires: A new fabrication method for nano-optics. *Nano Lett.* **2014**, *14*, 524−531.

(29) Fonseka, H. A.; Caroff, P.; Wong-Leung, J.; Ameruddin, A. S.; Tan, H. H.; Jagadish, C. Nanowires Grown On InP (100): Growth Directions, Facets, Crystal Structures, And Relative Yield Control. *ACS Nano* **2014**, *8*, 6945−6954.

(30) Friedl, M. G. Scalable Nanowire Networks: Growth and Functionality. Postdoctoral Thesis, EPFL, 2020.

(31) Coenen, T.; Haegel, N. M. Cathodoluminescence for the 21st century: Learning more from light. *Appl. Phys. Rev.* **2017**, *4*, 31103.

(32) Howe, J. M.; Fultz, B.; Miao, S. *Characterization of Materials*; John Wiley and Sons, Inc.: Hoboken, NJ, USA, 2012; pp 1−46.

(33) Brenny, B. J. M.; Abujetas, D. R.; van Dam, D.; Sánchez-Gil, J. A.; Rivas, J. G.; Polman, A. Directional Emission from Leaky and Guided Modes in GaAs Nanowires Measured by Cathodoluminescence. *ACS Photonics* **2016**, *3*, 677−684.

(34) Djemel, A.; Nouiri, A.; Kouissa, S.; Tarento, R.-J. Cathodoluminescence Calculation of n-GaAs. Surface Analysis and Comparison. *Phys. Status Solidi* **2002**, *191*, 223−229.

(35) Gustafsson, A. Nanowire-based structures for infrared to ultraviolet emitters studied by cathodoluminescence. *J. Microsc.* **2016**, *262*, 134−141.

(36) Zagonel, L. F.; Mazzucco, S.; Tencé, M.; March, K.; Bernard, R.; Laslier, B.; Jacopin, G.; Tchernycheva, M.; Rigutti, L.; Julien, F. H.; Songmuang, R.; Kociak, M. Nanometer scale spectral imaging of quantum emitters in nanowires and its correlation to their atomically resolved structure. *Nano Lett.* **2011**, *11*, 568−573.

(37) Zheng, C.; Wong-Leung, J.; Gao, Q.; Tan, H. H.; Jagadish, C.; Etheridge, J. Polarity-driven 3-fold symmetry of GaAs/AlGaAs core multishell nanowires. *Nano Lett.* **2013**, *13*, 3742−3748.

(38) Zhang, Y.; Sanchez, A. M.; Wu, J.; Aagesen, M.; Holm, J. V.; Beanland, R.; Ward, T.; Liu, H. Polarity-driven quasi-3-fold composition symmetry of self-catalyzed III-V-V ternary core-shell nanowires. *Nano Lett.* **2015**, *15*, 3128−3133.

(39) Guo, Y.-N.; Burgess, T.; Gao, Q.; Tan, H. H.; Jagadish, C.; Zou, J. Polarity-driven nonuniform composition in InGaAs nanowires. *Nano Lett.* **2013**, *13*, 5085−5089.

(40) De La Mata, M.; Magen, C.; Gazquez, J.; Utama, M. I. B.; Heiss, M.; Lopatin, S.; Furtmayr, F.; Fernández-Rojas, C. J.; Peng, B.; Morante, J. R.; Rurali, R.; Eickhoff, M.; Fontcuberta I Morral, A.; Xiong, Q.; Arbiol, J. Polarity Assignment in ZnTe, GaAs, ZnO, and GaN-AlN Nanowires From Direct Dumbbell Analysis. *Nano Lett.* **2012**, *12*, 2579−2586.

(41) Peña, F. d. l.; Prestat, E.; Fauske, V. T.; Burdet, P.; Lähnemann, J.; Furnival, T.; Jokubauskas, P.; Nord, M.; Ostasevicius, T.; MacArthur, K. E.; Johnstone, D. N.; Sarahan, M.; Aarholt, T.; Taillon, J.; Migunov, V.; Eljarrat, A.; Caron, J.; Poon, T.; Mazzucco, S.; Francis, C.; Martineau, B.; Somnath, S.; Slater, T.; Tappy, N.; Walls, M.; Cautaerts, N.; Winkler, F. *DENSmerijn, hyperspy/hyperspy*, Release v1.6.5., 2021 https://zenodo.org/record/5608741.

https://doi.org/10.1021/acsanm.2c00507
ACS Appl. Nano Mater. XXXX, XXX, XXX−XXX